PHYSICAL REVIEW A **84**, 053851 (2011)

Multispace quantum interference in a ^{57}Fe synchrotron Mössbauer source

G. V. Smirnov,[1,*] A. I. Chumakov,[2,1] V. B. Potapkin,[1,2,3] R. Rüffer,[2] and S. L. Popov[1]
[1]*National Research Centre "Kurchatov Institute", 123182 Moscow, Russia*
[2]*European Synchrotron Radiation Facility, F-38043 Grenoble, France*
[3]*Bayerisches Geoinstitut, Universität Bayreuth, D-95440 Bayreuth, Germany*

(Received 4 April 2011; published 28 November 2011)

A physical picture for coherent emission of γ rays by a nuclear array excited with synchrotron radiation is given. The particular case of a pure nuclear Bragg reflection from the ^{57}FeBO$_3$ crystal is analyzed. During free de-excitation of the nuclei, a nuclear exciton polariton is developing inside the crystal and generates at the exit of the crystal a coherent γ-ray beam. In the crystal the nuclear levels of ^{57}Fe are split because of a combined magnetic and electric interaction. The rich picture of γ-ray interference is described, which involves geometrical space, energy, and spin domains. In the vicinity of the Néel temperature of the crystal the magnetic splitting of nuclear levels nearly collapses. These conditions lead to drastic changes in the angular, energy, and temporal properties of the emitted radiation. The emission angular function, which in the approximation of a plane incident wave represents the emission intensity for different angular settings of the crystal near Bragg angle, strongly broadens and transforms to a double-hump structure with a central dip between the peaks. The energy and temporal distributions of the emitted radiation crucially depend upon the crystal angular setting. Beyond the central dip, the energy distribution of nuclear scattering acquires a complicated form with several satellites at various energies. In contrast, at the exact angular position of the central dip, the energy spectrum exhibits a single line shape with the line width close to the natural width of the nuclear resonance. The obtained results constitute the theoretical basis for the understanding and for the further elaboration of the ^{57}Fe synchrotron Mössbauer source—the device that provides a collimated beam of intense and polarized γ radiation in an energy bandwidth of nanoelectronvolts, the nuclear resonance natural level width.

DOI: 10.1103/PhysRevA.84.053851 PACS number(s): 42.25.Hz, 61.05.cc, 76.80.+y

I. INTRODUCTION

Hard x rays, generated by modern synchrotron radiation (SR) sources, can effectively excite low-lying nuclear metastable states. The short pulses of the x-ray photons provide an almost instantaneous, compared to the lifetime of nuclear state, knockwise excitation. Under these conditions, the processes of photon absorption and photon emission are two sequential, temporally decoupled, events. At the stage of free de-excitation, nuclei of a target generate recoilless γ radiation. This process can serve as an advantageous alternative to a conventional Mössbauer source. The physical nature of these two kinds of sources is, however, absolutely different.

Although in both the radioisotope and the SR-based source the same metastable states are excited and the de-excitation of them occurs spontaneously, the excited states are quite different in character and their decay modes differ drastically. In the radioisotope source only one single nucleus is excited at the time and thereafter emits radiation. In contrast, the excitation of nuclei by a SR pulse and the subsequent nuclear de-excitation are not localized at a single nucleus but spread out over a nuclear ensemble. In fact, each nucleus of the ensemble appears to be excited with a certain probability amplitude. In other words, the excitation is shared by all those nuclei. Such a state is referred to as nuclear exciton and can be perceived as a nuclear polarization wave. The initial phase distribution in a nuclear exciton is fully determined by the coherent properties of the transmitted radiation pulse. Typically, it is close to the phase distribution existing in a plane wave.

During de-excitation, each nucleus emits a partial γ-ray wavelet. Since all the wavelets are correlated in phase, their interference leads to the creation of the common coherent wave field. Inside a crystal, the nuclear polarization wave and the radiation field are tightly coupled and form together a self-consistent dynamical system, called *nuclear exciton polariton or nuclear polariton* [1–3]. As the nuclear polariton is developing, a γ-ray photon can be reabsorbed and re-emitted by nuclei several times. At the exit of the crystal, the nuclear polariton generates a γ-ray beam. The distribution of the emitted γ quanta in time and in space is dictated by the temporal and spatial development of the nuclear polariton, which can exist inside the target in forms of either running or standing wave. The running wave mode is realized in the processes of the forward scattering, while the standing-wave pattern is formed for nuclear Bragg reflections. The intensity of γ radiation emitted after each SR pulse is decaying in time. In space, the radiation usually forms the low-divergent beams both in the forward scattering and in Bragg reflection directions [4].

The delayed resonant γ radiation is, however, preceded by a high-intense x-ray pulse contributing a huge nonresonant background in the direction of the primary beam. Even after extreme monochromatization of the incident radiation (e.g., down to $\sim 10^{-3}$ eV) the signal-to-noise ratio is still 10^{-5}–10^{-6}(with the natural width of nuclear resonance $\Gamma_0 \sim 5$ neV). As for Bragg reflection, an x-ray photon can be reflected by a crystal through either nuclear resonant or Rayleigh electronic scattering processes. It is the electronic

---

[*] smirnov@polyn.kiae.su

scattering that brings the large background in the Bragg direction on top of the nuclear resonant signal.

Fortunately, the nature of nuclear Bragg reflections offers a way out of this disappointing situation. The solution of the problem can be found using electronically forbidden but nuclear-allowed Bragg reflections, which exist owing to an unusual polarization dependence of nuclear resonance scattering in the presence of hyperfine interaction. Such *pure nuclear reflections* were predicted for antiferromagnetic crystals [5,6] as well as for the crystals with electric field ordering [7], and observed in Refs. [8,9]. It was a pure nuclear reflection that was applied in the experiment where nuclear resonance excitation by synchrotron radiation was unequivocally observed [10].

Since the pure nuclear reflectivity is intimately related to magnetic or electric hyperfine interaction, the nuclear array in a crystal behaves as a multiline radiator due to hyperfine splitting of nuclear levels. This is, of course, an inconvenient characteristic of a Mössbauer source, which can not be accepted. Luckily, a particular case of hyperfine interaction, which is well matched to the idea of the generation of a single-line Mössbauer radiation, does exist. Pure nuclear reflectivity within an energy band of about the natural line width of the ^{57}Fe nuclear excited level has been obtained when an iron borate ^{57}FeBO$_3$ single crystal was heated close to Néel temperature T_N [11]. Temporal properties of pure nuclear diffraction in the vicinity of T_N were studied in Ref. [12] using the pulsed structure of SR.

Approaching the transition to the paramagnetic state at Néel temperature (for ^{57}FeBO$_3$ T_N is ∼348 K), the hyperfine structure of the Mössbauer diffraction spectrum for ^{57}FeBO$_3$ collapses and the reflection normally disappears above T_N due to destructive spatial interference. However, an application of an external weak magnetic field to the crystal results in a drastic transformation of the interference conditions. According to the quantum mechanical principle of superposition of states, after absorption of a SR x-ray photon every nucleus of the nuclear ensemble can be found on one of the four allowed sublevels of the excited state. Furthermore, due to mixing the nuclear spin states, each of these four sublevels is characterized by two allowed spin projections. Thus, the emission of a delayed gamma-ray photon is described by the multispace interference of the relevant probability waves, where geometrical, energy, and spin domains are intrinsically involved. The combined multipath interference in space, energy, and spin domains results in a pseudosingle-line resonance structure, which provides a basis for the creation of a single-line synchrotron Mössbauer (SM) source. An analysis of the hyperfine structure under these conditions is given in Ref. [13].

The source of SR-based Mössbauer radiation has been developed [14] in 1997 at the European Synchrotron Radiation Facility. The source emits a directed beam of fully recoilless and polarized radiation. These properties have been effectively used in the application of the SM source for studying magnetic field distribution in iron alloys [15]. Significant progress in the further development of the SM source has recently been achieved at SPring-8 [16].

The physics of SMS is a fascinating example of multispace quantum interference (i.e., the interference of a gamma-quantum in geometrical, energy, and spin spaces). This paper is devoted to the detailed analysis of these coherent processes, which determine the properties of the SM radiation. Namely, the angular, energy, and time distributions of the SM radiation are analyzed in order to define necessary conditions for an optimal performance of the SM source. The remainder of the paper is organized as follows. Section II gives a detailed analysis of the process of the multispace interference of nuclear resonant scattering of SR by the unit cell of ^{57}FeBO$_3$. In Sec. III, properties of the nuclear polariton for the diffraction process of γ radiation by the nuclear array are considered. In Sec. IV, the angular, energy, and time distributions of the ^{57}Fe SM radiation are calculated. A summary is given in Sec. V.

II. MULTISPACE INTERFERENCE OF γ-RAY PHOTON IN THE UNIT CELL OF ^{57}FeBO$_3$ CRYSTAL

We consider the emission of a γ-ray photon by the two ^{57}Fe nuclei belonging to the unit cell of ^{57}FeBO$_3$, iron borate (IB), crystal. Let the nuclei be excited by a short pulse of synchrotron radiation much shorter than the lifetime of the excited nucleus. Then the processes of nuclear excitation and de-excitation are two sequential, temporally well decoupled, events. After the prompt absorption of a primary photon and some dwelling in the intermediate excited state, the transition back to the ground state occurs with emission of a secondary photon. In accordance with the general principles of excitation, both nuclei are excited in the intermediate state with equal probability amplitudes, the phases of which in the case of a plane synchrotron radiation wave are determined by the scalar product $\mathbf{k}_i\mathbf{r}_a$, where $\mathbf{k}_i$ is the wave vector of the incident radiation and $\mathbf{r}_a$ is the vector indicating the position of a nucleus in the unit cell ($a = 1,2$). In order to calculate the emission in the direction $\mathbf{k}_f$, one should add up the amplitudes of the two γ-ray wavelets with the account of their relative phase, which is determined by the difference in their corresponding optical paths. The phase difference is then given by the expression $(\mathbf{k}_f - \mathbf{k}_i)(\mathbf{r}_2 - \mathbf{r}_1)$. Thus, in order to evaluate the result of the interference in geometrical space, one has to consider two paths. The phase difference of waves scattered along the two paths plays a crucial role for the intensity of emission.

Each of the two spatial paths is branched further into separate paths within the energy domain. Due to magnetic dipole interaction of the nuclear spin with the internal field, the nuclear levels in the IB crystal are split into sublevels. The level of the ground state having nuclear spin $I_g = \frac{1}{2}$ splits into two sublevels; and the level of the excited state having spin $I_e = \frac{3}{2}$ splits into four sublevels. The selection rules for magnetic dipole transition (M1), relevant to our case, allow one to observe six nuclear transitions between the ground and excited states with the change of the magnetic quantum number $M = m_e - m_g = 0,\pm 1$. Here m_e, m_g are the magnetic quantum numbers for the excited and ground nuclear states, respectively.

The IB crystal is a canted antiferromagnet. The magnetic and crystalline unit cells of the crystal are the same (as for Fe$_2$O$_3$ hematite crystal, see Fig. 16 in Ref. [17]). The

TABLE I. Nuclear transitions between the ground and excited states with magnetic quantum numbers $m_e \to m_g$ for various transition energies E_n^{trans} and various nuclei a in the unit cell of the IB crystal.

a	E_1^{trans}	E_2^{trans}	E_3^{trans}	E_4^{trans}	E_5^{trans}	E_6^{trans}
1	$-\frac{1}{2} \to -\frac{3}{2}$	$-\frac{1}{2} \to -\frac{1}{2}$	$-\frac{1}{2} \to +\frac{1}{2}$	$+\frac{1}{2} \to -\frac{1}{2}$	$+\frac{1}{2} \to +\frac{1}{2}$	$+\frac{1}{2} \to +\frac{3}{2}$
2	$+\frac{1}{2} \to +\frac{3}{2}$	$+\frac{1}{2} \to +\frac{1}{2}$	$+\frac{1}{2} \to -\frac{1}{2}$	$-\frac{1}{2} \to +\frac{1}{2}$	$-\frac{1}{2} \to -\frac{1}{2}$	$-\frac{1}{2} \to -\frac{3}{2}$

magnetic fields acting upon nuclei in the unit cell are equal in magnitude but almost opposite in direction. For this reason, the sublevels of the excited and the ground states have the same energies for both nuclei but the states appropriate to the equivalent sublevels are characterized by the opposite signs of the magnetic quantum numbers. Therefore, the transitions at the first and second nuclei with the same resonant transition energies (E_n^{trans}) have the opposite signs in the change M of the spin magnetic quantum numbers (see Table I). Here the spin quantization axis z is chosen to be directed along the magnetic field at the first nucleus.

For each arbitrary energy E^{trans} of the radiation spectral component all six transitions will give their specific contributions to the interference field depending on the energy distance between E^{trans} and a resonant energy E_n^{trans}, where $n = 1,2,\ldots,6$. Here one definitely faces a bright case of *inter-resonance nuclear interference*. For the Lorentzian shape of each resonance, the summary amplitude of scattering is then proportional to $\sum_{n=1}^{6} \frac{1}{v_n - i}$, where $v_n = (E^{\text{trans}} - E_n^{\text{trans}})/(\Gamma_0/2)$ stands for the energy deviation from the nth resonance in the units of the resonance natural half-width (for the sake of simplicity we have assumed so far that the amplitudes of different transitions are equal to each other). Thus, for the two nuclei in the unit cell the combined process of γ-ray interference in geometrical and energy spaces involves twelve contributions.

The arrangement of atoms in the IB crystal does not only result in the formation of the internal magnetic field at the iron sites but also in the creation of a nonuniform crystalline electric field. The electric field gradient (EFG) in the crystal exhibits axial symmetry. The principal axis of the EFG tensor is orthogonal to the internal magnetic field at both iron sites. The ^{57}Fe nucleus in the first excited state possesses both a magnetic and a quadrupole moment, while in the ground state it has only a magnetic moment. So, the nucleus experiences a pure magnetic dipole interaction in the ground state and a combined magnetic dipole and axially symmetric electric quadrupole interaction in the excited state.

The splitting of nuclear states in an IB crystal under conditions of the combined magnetic dipole and electric quadrupole hyperfine interaction has been analyzed in Ref. [13]. The four dimensionless energies ε of the hyperfine interaction in the excited state are given by

$$\begin{aligned} \varepsilon_{1,3} &= +\tfrac{1}{2}\nu \pm \sqrt{\nu^2 - 3\nu + 9}, \\ \varepsilon_{2,4} &= -\tfrac{1}{2}\nu \pm \sqrt{\nu^2 + 3\nu + 9}, \end{aligned} \tag{1}$$

where $\nu = \omega_B/\omega_E, \hbar\omega_B = g_e \mu_n B$ is the energy of interaction of the magnetic moment of the nucleus in the excited state with the internal magnetic field B (g_e is the nuclear g factor in the excited state, μ_n is the nuclear magneton) and $\hbar\omega_E = \frac{1}{2} e Q \frac{\partial^2 V_{\text{el}}}{\partial y^2} \frac{1}{2I_e(2I_e - 1)}$ is the energy of interaction of the nuclear electric quadrupole moment Q with the electric field gradient (V_{el} is the electric field potential at the nucleus, e is the charge of proton); ε_i are given in the units of the quadrupole interaction energy $\hbar\omega_E$. Since in the excited state of ^{57}Fe the g factor is negative, the sublevel energies are ordered in the following way: $\varepsilon_1 \leqslant \varepsilon_2 \leqslant \varepsilon_3 \leqslant \varepsilon_4$. Concerning the value of the internal magnetic field, it is a function not only of temperature but also of the applied magnetic field. The application of the external field plays a significant role in the near vicinity of Néel temperature where antiferromagnetic ordering of the atomic spins can be induced in the crystal [18].

For pure magnetic interaction pure spin states (i.e., the states with a defined spin projection m) can exist. But under conditions of combined magnetic and electric hyperfine interaction the excited nuclear states may be mixed over the spin projections. In the particular case of the axially symmetric EFG with the main axis orthogonal to the magnetic field and z axis directed along the magnetic field, each nuclear excited state is mixed over two spin projections. In this case the Hamiltonian eigenvalues given by Eq. (1) are appropriate for the eigenfunctions of the excited states represented in Table II.

The excited nuclear states with energies ε_1, ε_3 are mixed over spin projections $+\frac{1}{2}, -\frac{3}{2}$, whereas the states with energies ε_2, ε_4 are mixed over spin projections $-\frac{1}{2}, +\frac{3}{2}$. Table II shows that only four amplitudes $\alpha_1,\alpha_2,\alpha_3,\alpha_4$ are required to describe the eigenfunctions of all excited states for both nuclei. Following the analysis presented in Ref. [13],

TABLE II. The mixed-spin eigenfunctions for various excited nuclear states with the eigen energies ε_i and for various nuclei a in the unit cell of the IB crystal.

a	ε_1	ε_2	ε_3	ε_4
1	$\alpha_1\lvert -\frac{3}{2}\rangle + \alpha_2\lvert +\frac{1}{2}\rangle$	$\alpha_3\lvert -\frac{1}{2}\rangle + \alpha_4\lvert +\frac{3}{2}\rangle$	$\alpha_1\lvert +\frac{1}{2}\rangle + \alpha_2\lvert -\frac{3}{2}\rangle$	$\alpha_3\lvert +\frac{3}{2}\rangle + \alpha_4\lvert -\frac{1}{2}\rangle$
2	$\alpha_1\lvert +\frac{3}{2}\rangle + \alpha_2\lvert -\frac{1}{2}\rangle$	$\alpha_3\lvert +\frac{1}{2}\rangle + \alpha_4\lvert -\frac{3}{2}\rangle$	$\alpha_1\lvert -\frac{1}{2}\rangle + \alpha_2\lvert +\frac{3}{2}\rangle$	$\alpha_3\lvert -\frac{3}{2}\rangle + \alpha_4\lvert +\frac{1}{2}\rangle$

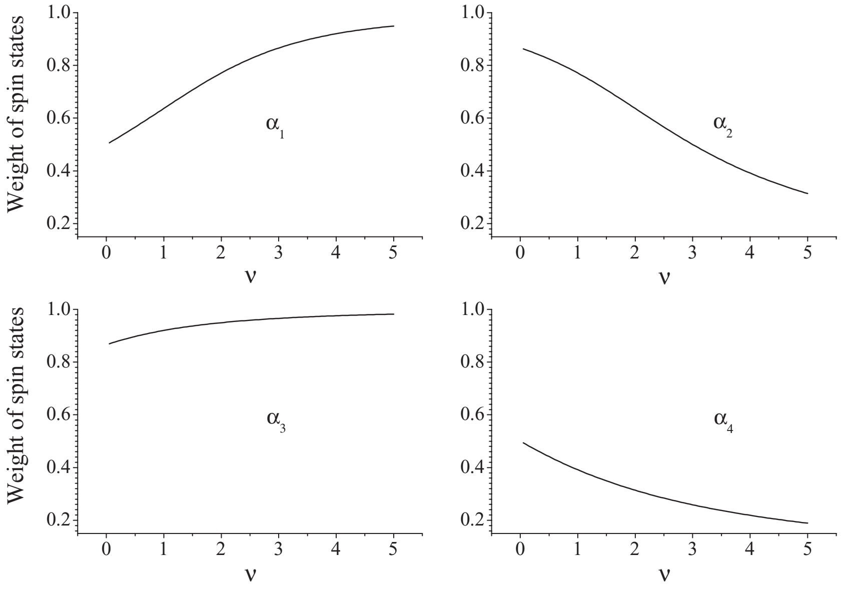

FIG. 1. Amplitudes α_{1-4} of contributions of the pure spin states $|\pm\frac{1}{2}\rangle$, $|\pm\frac{3}{2}\rangle$ into the mixed spin states for different energy sublevels ϵ_{1-4} of the excited nuclear state of different nuclei in the unit cell of the IB crystal (see Table II). For parameter ν see explanation to Eq. (1).

these amplitudes can be obtained in an explicit form

$$\begin{aligned}
\alpha_1 &= \frac{1}{\sqrt{A_1^2/27+1}}, \quad & A_1 &= 2\nu - 3 - 2\sqrt{\nu^2 - 3\nu + 9},\\
\alpha_2 &= \frac{1}{\sqrt{A_2^2/27+1}}, \quad & A_2 &= 2\nu - 3 + 2\sqrt{\nu^2 - 3\nu + 9},\\
\alpha_3 &= \frac{1}{\sqrt{A_3^2/27+1}}, \quad & A_3 &= 2\nu + 3 - 2\sqrt{\nu^2 + 3\nu + 9},\\
\alpha_4 &= \frac{1}{\sqrt{A_4^2/27+1}}, \quad & A_4 &= 2\nu + 3 + 2\sqrt{\nu^2 + 3\nu + 9}.
\end{aligned} \tag{2}$$

They are defined by a single parameter $\nu = \omega_B/\omega_E$. The magnetic hyperfine field in the IB crystal is a function of temperature. Approaching the transition to the paramagnetic state at Néel temperature T_N, the field magnitude B rapidly decreases. At room temperature, the magnetic interaction dominates over the electric one, parameter $\nu \simeq 90$, and the excited nuclear states are nearly pure spin states with $\alpha_1 \simeq \alpha_3 \simeq 1$ and $\alpha_2 \simeq \alpha_4 \simeq 0$. In contrast, in the range of $\nu < 10$ the excited states are already significantly mixed over spin projections. The evolution of the mixed-spin states is illustrated in Fig. 1. The dependencies of the pure spin state contributions α_{1-4} into the mixed states are shown within the range of $\nu < 5$, where the magnetic dipole and electric quadrupole hyperfine interactions are becoming comparable. Figure 1 clearly shows that in approaching Néel temperature ($\nu \to 0$), the excited states are getting strongly mixed over spin projections. Because the two spin projections are mixed in each excited substate the resonance scattering via a separate nuclear transition in every nucleus branches out further into the four paths.

For elastic scattering, the process considered here, the initial and final states are the same. Therefore, if measurements do not permit to establish which intermediate spin state was involved in the scattering, the scattering paths related to all intermediate states should interfere. Here one meets an interesting case of *intraresonance nuclear interference* in the spin domain. Figure 2 shows an example of the scattering paths via the nuclear transition with the lowest transition energy E_1^{trans} for the first nucleus. As it is seen from the figure, in order to build up the interference field for a given transition in a single nucleus, four wavelets of the same frequency but different in polarization states and scattering amplitudes should be added.

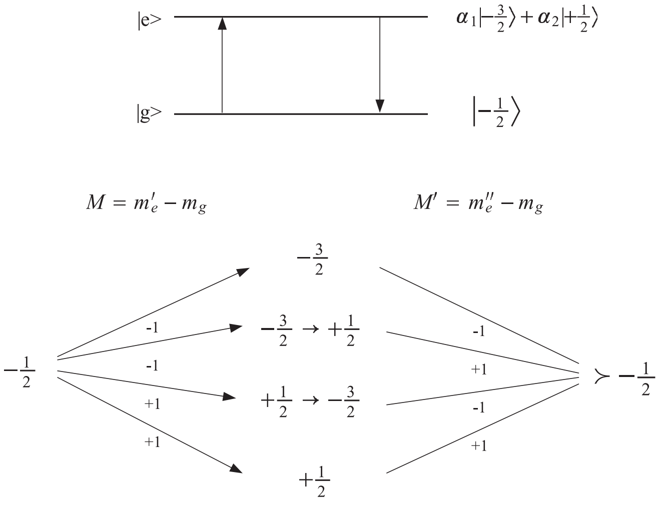

FIG. 2. Scattering paths via the pure spin states of the excited nuclear substate having energy ε_1 in the first nucleus of the IB crystal unit cell. On the upper panel the transitions, up and down, between the ground and the excited states are displayed. On the lower panel four possible paths are shown, where changes of spin projections in different paths are indicated. $M = m_e - m_g = \pm 1$ are the changes of magnetic quantum number in separate transitions; m_e,m_g are the magnetic quantum numbers for the excited and ground nuclear states respectively.

The amplitude of a wavelet for nth nuclear transition in ath nucleus contains the complex G^a_n factor given by the following general expression:

$$G^a_n(m'_e,m''_e) = \langle \tfrac{1}{2},m_g;1,M|\tfrac{3}{2},m'_e\rangle \langle \tfrac{1}{2},m_g;1,M'|\tfrac{3}{2},m''_e\rangle c_j^{m'_e} c_j^{m''_e} \times \left(\mathbf{h}^s_d \mathbf{u}^a_{-M}\right)\left(\mathbf{h}^{s'}_{d'}\mathbf{u}^a_{-M'}\right)^*, \tag{3}$$

where $\langle \frac{1}{2},m_g;1,M|\frac{3}{2},m_e\rangle$ designates a Clebsch–Gordan coefficient, which is a probability factor for the transition between sublevels of the ground and excited states taking into account the angular momentum transfer for the (nucleus + photon) system; it also depends on the spins of the ground and the excited states and on their z projections. In this manuscript we are considering diffraction with (M1) multipolarity (magnetic dipole transition) and have chosen the magnetic basis for the polarization vector. $(\mathbf{h}^s_d\mathbf{u}^a_{-M})$ is the scalar product of the magnetic polarization vector $\mathbf{h}^s_d$ of the wave propagating in the direction $d = 0,1$ (0 stands for the direction along the incident wave, 1 for the direction along the exit wave), with polarization $s = \pi,\sigma$ (vectors $\mathbf{h}^\sigma_{0,1}$ lie in the scattering plane, while vectors $\mathbf{h}^\pi_{0,1}$ are perpendicular to it) and the spherical unit vector $\mathbf{u}^a_{-M}$ in the coordinate system related to the hyperfine fields at the ath nucleus in the unit cell. $\mathbf{u}^a_0 = \mathbf{u}^a_z$, $\mathbf{u}^a_{\pm1} = \mp\frac{1}{\sqrt{2}}(\mathbf{u}^a_x \pm i\mathbf{u}^a_y)$, where $\mathbf{u}_{x,y,z}$ are mutually orthogonal unit vectors related to the hyperfine fields in the unit cell, $\mathbf{u}_z$ is directed along vector $\mathbf{B}$ (see Fig. 3). Finally, $c_j^{m_e}$ are the amplitudes of spin states in the jth sublevel of the excited nuclear state. Below the $c_j^{m_e}$ amplitudes are related to the defined above α amplitudes.

$$\begin{aligned} c_1^{-\frac{3}{2}} &= c_1^{+\frac{3}{2}} = c_3^{+\frac{1}{2}} = c_3^{-\frac{1}{2}} = \alpha 1,\\ c_1^{+\frac{1}{2}} &= c_1^{-\frac{1}{2}} = c_3^{-\frac{3}{2}} = c_3^{+\frac{3}{2}} = \alpha 2,\\ c_2^{-\frac{1}{2}} &= c_2^{+\frac{1}{2}} = c_4^{+\frac{3}{2}} = c_4^{-\frac{3}{2}} = \alpha 3,\\ c_2^{+\frac{3}{2}} &= c_2^{-\frac{3}{2}} = c_4^{-\frac{1}{2}} = c_4^{+\frac{1}{2}} = \alpha 4. \end{aligned} \tag{4}$$

In the example, depicted in Fig. 2, the interference in spin space leads to the following expression of the G^1_1 factor:

$$\begin{aligned} G^1_1 = {} & \frac{1}{2}\,\alpha_1^2\left(\mathbf{h}^s_d\mathbf{u}^1_{+1}\right)\left(\mathbf{u}^{s'}_{d'}\mathbf{u}^1_{+1}\right)^* + \frac{1}{2\sqrt{12}}\alpha_1\alpha_2\left(\mathbf{h}^s_d\mathbf{u}^1_{+1}\right)\left(\mathbf{h}^{s'}_{d'}\mathbf{u}^1_{-1}\right)^*\\ & + \frac{1}{2\sqrt{12}}\alpha_2\alpha_1\left(\mathbf{h}^s_d\mathbf{u}^1_{-1}\right)\left(\mathbf{h}^{s'}_{d'}\mathbf{u}^1_{+1}\right)^*\\ & + \frac{1}{12}\alpha_2^2\left(\mathbf{h}^s_d\mathbf{u}^1_{-1}\right)\left(\mathbf{h}^{s'}_{d'}\mathbf{u}^1_{-1}\right)^*. \end{aligned} \tag{5}$$

This example explicitly shows that the result of interference in spin space is strongly dependent on the amplitudes α_j of the pure spin substates in the mixed state, which are functions of the crystal temperature. In order to derive the intensity of the emitted radiation, one needs to calculate the nuclear susceptibility amplitude η taking into account all the mentioned interference paths according to the following expression:

$$\eta^{ss'}_{dd'} = -\frac{3}{KV_0}\sigma_0\beta f_{LM}\sum_a \exp\{i\,(\mathbf{k}_{d'}-\mathbf{k}_d)\,\mathbf{r}_a\} \times \sum_n \frac{1}{\upsilon_n - i}\sum_{m'_e,m''_e} G^a_n(m'_e,m''_e). \tag{6}$$

The outermost summation here represents the internuclear interference of scattering by different nuclei in the unit cell, the medium summation represents the inter-resonance nuclear interference of scattering via the transitions between the various sublevels of the ground and the excited states, and the innermost summation represents the intraresonance nuclear interference in the transitions via the various spin states of a particular excited nuclear substate.

In Eq. (6) $K = 2\pi/\lambda$ stands for the radiation wave number in vacuum; V_0 is the volume of the crystal unit cell; σ_0 is the resonance cross section; β is the resonant isotope abundance; f_{LM} is the recoilless scattering factor, which is the product of square roots of the Lamb-Mössbauer factors in the directions d,d'; $\mathbf{k}_d$ and $\mathbf{k}_{d'}$ are the wave vectors of the incident and exit waves, respectively. In general the nuclear susceptibility amplitudes form a matrix with dimensions (4 × 4). Altogether,

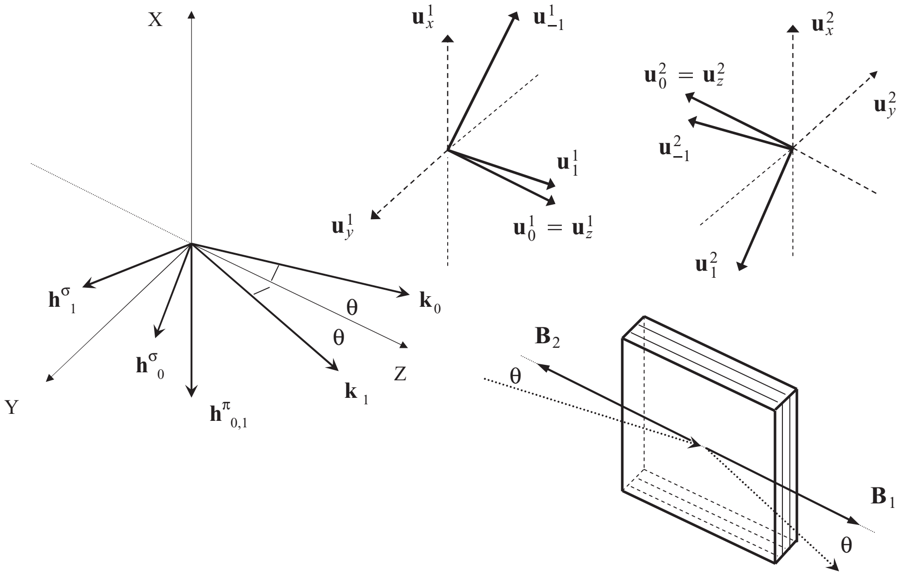

FIG. 3. Scattering geometry of synchrotron radiation from two nuclei in the IB crystal unit cell; $\mathbf{k}_{0,1}$ and $\mathbf{h}^{\pi,\sigma}_{0,1}$ are the wave vectors and the magnetic polarization vectors of the incident and scattered waves respectively, θ is incidence angle (symmetric scattering geometry is considered); $\mathbf{B}_{1,2}$ are the magnetic fields at the nuclei in the unit cell; $\mathbf{u}^{1,2}_{0,1,-1}$ are the spherical unit vectors related to hyperfine fields at the first and second nuclei in the IB crystal unit cell (see text for definition).

the combined γ-ray interference process in the geometrical, energy, and spin spaces should involve 48 contributions.

In the IB crystal pure nuclear diffraction occurs for the reflections with an odd sum of the Miller indexes, in particular, for reflections (111), (333) etc. These are symmetric reflections because IB crystals grow as platelets with surface planes parallel to the (111) crystallographic plane. We consider the horizontal scattering geometry. That is illustrated in Fig. 3, where the polarization and wave vectors of the incident and scattered waves and the sets of the spherical unit vectors at each nucleus in the unit cell are depicted. The magnetic fields at the nuclei lie in the scattering plane.

Synchrotron radiation is linearly polarized. The magnetic polarization vector $\mathbf{h}_0^\pi$ is perpendicular to the scattering plane. The internal magnetic fields $\mathbf{B}_{1,2}$ are orthogonal to the magnetic polarization vector. In the chosen geometry, the susceptibility amplitudes matrix is reduced to a matrix of second rank. For the π-polarized incident radiation, it takes the following form:

$$\eta_{dd'}^{ss'} = \begin{vmatrix} \eta_{00}^{\pi\pi} & \eta_{01}^{\pi\sigma} \\ \eta_{10}^{\sigma\pi} & \eta_{11}^{\sigma\sigma} \end{vmatrix}. \tag{7}$$

In the presence of hyperfine interaction a nuclear array may act as an optically active medium for incident γ radiation. In particular, because of the antiferromagnetic arrangement of the fields at the nuclei in the unit cell of the IB crystal, the polarization plane under conditions of pure nuclear diffraction is turned through angle $\pi/2$, so that the exit wave is σ polarized. In the next section we consider the coherent scattering of the γ-ray by the whole nuclear array in the crystal.

III. NUCLEAR EXCITON POLARITON UNDER DIFFRACTION CONDITIONS

A nuclear array in a crystal represents for Mössbauer radiation a resonating three-dimensional grating, which gives rise to resonant Bragg diffraction of γ-rays. If regularity of the grating persists over a large volume of the crystal, the multiple scattering of radiation occurs. Mutual interference of the propagating and Bragg reflected waves produces a resultant wave field the structure of which is of a standing-wave type. In this way the standing-wave mode of nuclear exciton polariton is realized under conditions of Bragg diffraction. At the exit of the crystal a coherent beam of resonant γ radiation is formed. In general, the Bragg diffraction in large perfect crystals is described by the dynamical theory accounting for the multiple scattering of radiation by atoms. The dynamical theory for nuclear resonant scattering was developed by different groups using different approaches. A detailed account of the dynamical diffraction theory of nuclear resonant diffraction is given by Kagan, Trammell, and Hannon in their reviews [19,20]. We shortly summarize the theory based on the solution of the Maxwell equations and apply it to our case.

The existence of the nuclear exciton provides the physical basis for the use of a macroscopic polarization, which is given by the Maxwell equations to treat the radiative effects of the nuclei. The induced nuclear current density represents then a quantum mechanical average over the nuclear ensemble. For a space and time Fourier component of the electric-field vector $\mathbf{E}(\mathbf{k},\omega)$, which represents the amplitude of a plane monochromatic γ-ray wave having the wave vector $\mathbf{k}$ and frequency ω, the Maxwell wave equation can be written in the following form:

$$[k^2 - K^2]\mathbf{E}(\mathbf{k},\omega) - \mathbf{k}[\mathbf{k}\cdot\mathbf{E}(\mathbf{k},\omega)] = \frac{4\pi i\omega}{c^2}\mathbf{j}(\mathbf{k},\omega), \tag{8}$$

where K and k are the radiation wave numbers in vacuum and inside the crystal, respectively, $\mathbf{j}(\mathbf{k},\omega)$ is the Fourier component of the induced current density. It has contributions from both the electric and nuclear subsystems. But our interest is focused on the pure nuclear reflections. In this case the interference field is created only by nuclear currents and the above equation is in fact the equation for a space-time Fourier component of the nuclear polariton where the radiation field and nuclear excitation are related. In the linear in-field approximation the excited nuclear current $\mathbf{j}(\mathbf{k},\omega) \propto \eta\cdot\mathbf{E}(\mathbf{k},\omega)$ is proportional to the nuclear susceptibility amplitude. Employing this relationship one can arrive at the Maxwell equation for the field amplitude only. For the two-waves diffraction case the Maxwell wave equation splits into a set of two equations and in the conditions described in the previous section the equations set acquires the form

$$\begin{aligned} \left(\frac{k_0^2}{K^2} - 1\right) E_0^\pi &= \tilde{\eta}_{00}^{\pi\pi} E_0^\pi + \eta_{01}^{\pi\sigma} E_1^\sigma, \\ \left(\frac{k_1^2}{K^2} - 1\right) E_1^\sigma &= \eta_{10}^{\sigma\pi} E_0^\pi + \tilde{\eta}_{11}^{\sigma\sigma} E_1^\sigma, \end{aligned} \tag{9}$$

where E_d^s is the scalar electric field amplitude of a definite wave polarization and propagation direction, k_0 and k_1 are the complex wave numbers describing the coherent waves inside the crystal, and $\eta_{dd'}^{ss'}(\omega)$ are the nuclear susceptibility amplitudes considered above (radiation frequency $\omega = E^{\text{trans}}/\hbar$), the amplitudes labeled by tilde include the electronic susceptibility amplitudes. Electrons add their contribution only into 00 and 11 scattering channels. The complex wave numbers $k_{0,1}$ differ from the absolute value of the wave vector in vacuum K by only small complex corrections

$$k_0 = K(1+\epsilon_0), \quad k_1 = K(1+\epsilon_1). \tag{10}$$

In the vicinity of the Bragg angle $\epsilon_1 = \alpha/2 + \epsilon_0/\beta$, where $\alpha = -2\sin 2\theta_B \Delta\theta$ is the angular parameter proportional to the deviation $\Delta\theta$ from the Bragg angle θ_B and β is asymmetry parameter, $\beta = -1$ in the case of symmetric Bragg diffraction. With the account of the relations Eq. (10) we arrive at the following equations set (neglecting the small order values):

$$\begin{aligned} 2\epsilon_0 E_0 &= \tilde{\eta}_{00} E_0 + \eta_{01} E_1, \\ (-2\epsilon_0 + \alpha) E_1 &= \eta_{10} E_0 + \tilde{\eta}_{11} E_1, \end{aligned} \tag{11}$$

where polarization indexes are omitted. The equations (11) have a solution for the scalar field amplitudes only if the determinant formed by their coefficients vanishes

$$\begin{bmatrix} \tilde{\eta}_{00} - 2\epsilon_0 & \eta_{01} \\ \eta_{10} & \tilde{\eta}_{11} + 2\epsilon_0 - \alpha \end{bmatrix} = 0. \tag{12}$$

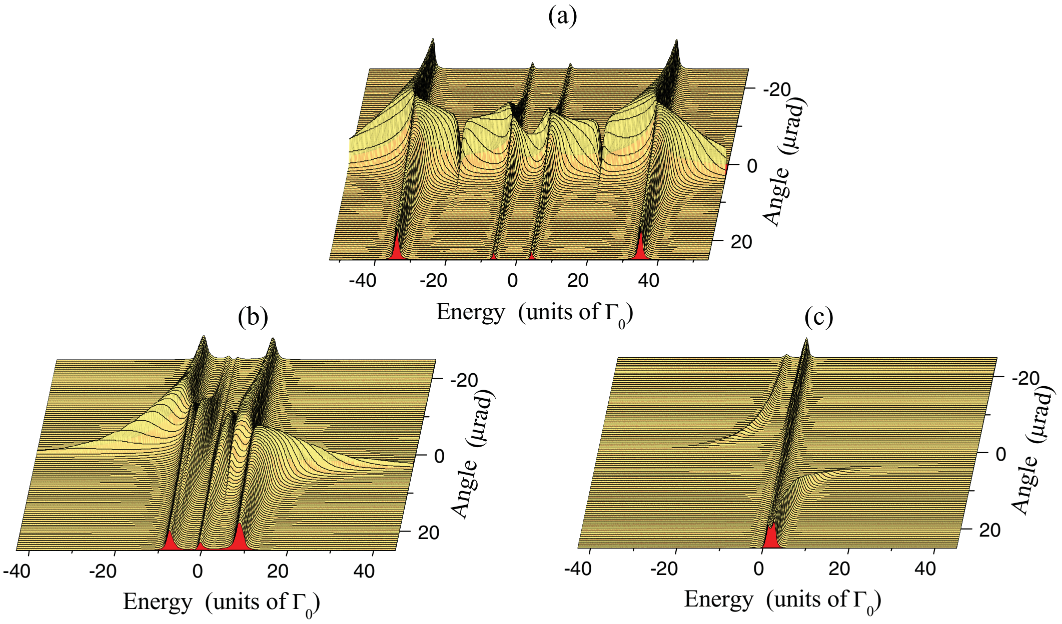

FIG. 4. (Color online) Evolution of the γ-ray emission landscape. The internal magnetic field at ^{57}Fe nuclei positions is: (a) 330 KOe, (b) 50 kOe, (c) 2 kOe.

Eq. (12) determines the dispersion of the electromagnetic waves in the crystal, giving the complex value ϵ_0 as a function of the radiation frequency ω and of the angular deviation α from the exact Bragg position. There are two roots of the Eq. (12)

$$\epsilon_0^{(1,2)} = \tfrac{1}{4}\{(\tilde{\eta}_{00} - \tilde{\eta}_{11} + \alpha)\} \mp \sqrt{(\tilde{\eta}_{00} + \tilde{\eta}_{11} - \alpha)^2 - 4\eta_{10}\eta_{01}}. \tag{13}$$

Thus one should consider the two standing-wave solutions for the interference wave fields WF1 and WF2, each corresponds to a particular dispersion correction $\epsilon_0^{(1)}$ or $\epsilon_0^{(2)}$. Substituting ϵ_0 from Eq. (13) into Eq. (11) one can find solutions for the relevant pairs of the scalar amplitudes. Since Eqs. (11) are homogeneous one has to use in addition the boundary conditions for the scalar amplitudes. Finally one arrives at the solutions for the WF amplitudes where the latter are modulated in the direction perpendicular to the reflecting planes in such a way that WF1 experiences an anomalously weak nuclear absorption, while WF2 on the contrary experiences an anomalously strong absorption. In the limit of a semi-infinite crystal only the WF1 survives. A strong suppression of inelastic scattering channels for this wave field is favoring an enhanced γ-ray emission nearly without the internal conversion (see Refs. [21,22]). The solution for the emitted radiation in this case is as follows:

$$E(\alpha,\omega) = \frac{\eta_{10}}{2\epsilon_0^{(1)} - \tilde{\eta}_{00}} E_{\mathrm{SR}}, \tag{14}$$

where $E_{\mathrm{SR}} = \sqrt{I_{\mathrm{SR}}/\Delta\omega}$ is the scalar amplitude of the SR with I_{SR} as the intensity of SR within the frequency range $\Delta\omega$ selected by the monochromator system.

For nuclear resonant Bragg reflections the emission from a crystal containing a nuclear array exhibits a combined angular and energy dependence.

A three-dimensional landscape of a Bragg reflection in the vicinity of the nuclear resonance and of the Bragg angle is formed. In the case of the IB crystal the landscape undergoes dramatic changes while heating the crystal from room to Néel temperature. The transformation of the energy-angular landscape is seen from Fig. 4. The emission intensity functions $I(\alpha,\omega) = |E(\alpha,\omega)|^2$ are displayed there for the actual scattering geometry (see Fig. 3) in the case of the pure nuclear reflection (333) for three different values of the internal magnetic field: 330 kOe ($\nu \approx 87$) in Fig. 4(a), 50 kOe ($\nu \approx 13$) in Fig. 4(b), and 2 KOe ($\nu \approx 0.5$) in Fig. 4(c). The energy scales cover the range of characteristic hyperfine interaction in ^{57}FeBO$_3$ and the angular scales cover the characteristic range of nuclear Bragg reflection (333) in the iron borate single crystal. The four well-separated crests, extended along the angular coordinate are seen in Fig. 4(a), each belongs to one of the allowed transitions with $M = \pm 1$ at the relevant transition energies $E_{1,3,4,6}^{\mathrm{trans}}$ (see Table I). The angular scale is centered at the Bragg angle. Far from the Bragg angle the four isolated resonance peaks (i.e., resonance lines) are formed. In approaching the Bragg angle the resonances exhibit an impressive broadening: the resonance lines with widths of several tenths of Γ_0 are getting overlapped in this angular range. This is an exciting result of a strong coherent enhancement of the radiative channel [23,24]. Because of the resonance broadening the inter-resonance interference starts playing the essential role even at room temperature. On the overlapping slopes of the first and the thrid lines, as well as of the fourth and the sixth lines the deep and sharp valleys (i.e., minima of the scattered intensity) are observed, which are due to the resonance absorption of γ radiation at the energies $E_{2,5}^{\mathrm{trans}}$. For the transitions $\mathrm{M} = 0$ the nuclear diffraction is cancelled due to destructive interference of the constituting waves in geometric space.

When due to the crystal heating the internal field decreases down to 50 kOe, the role of the inter-resonance interference rises significantly, Fig. 4(b). The effect of the interference is seen in a much broader angular range. The interference causes a strong asymmetry in both energy and angular distribution of the emitted radiation. Beyond the Bragg angle range the energy spectrum contains only three peaks at the lower angles: The third line is suppressed there, while at the higher angles the four lines are present but with the strongly weakened inner ones. Within the Bragg angle range a complicated interference pattern is observed where one can still distinguish the four lines of about equal strength. On the energy scale, off the resonance range far extended wings attract attention. They are also present on the former figure. The wings represent an axial symmetric configuration. Such a symmetry is due to varying conditions of the interference of the waves scattered by nuclei and is related to the fact that the real part of the nuclear amplitude is uneven function of the energy deviation from resonance.

Finally, we come near to the Néel point with the magnetic field of only 2 kOe [Fig. 4(c)]. The multiline spectrum of the emitted radiation has significantly collapsed here. In the vicinity of the Bragg angle a pseudosingle-line resonance structure is observed, which is created by the destructive internuclear interference (in geometrical space) as well as by a strong inter-resonance (in energy domain) and intraresonance (in spin domain) interference of radiation components discussed in the preceding section.

As seen in Fig. 4 emission occurs over a range of settings of the crystal around the Bragg angle. To reveal the details of the interference pattern in the following section we have analyzed the angular function of the coherent emission and determined the angular breadth of strong emission for different magnitudes of the internal magnetic field. In addition the spectral composition and the time distribution of γ-ray photons radiated by the nuclear array in the SM source were examined.

IV. ANGULAR, ENERGY, AND TIME DISTRIBUTIONS OF ^{57}Fe SM RADIATION

Initially we discuss the geometrical properties of the interference pattern. First of all we wish to know how the intensity of the γ radiation emitted by the crystal depends on its angular setting in the vicinity of the Bragg angle. To estimate the theoretical angular width of the emission function for a perfect crystal we can neglect the angular width of the incident beam, assuming a plane wave is incident on the crystal. To find in this way the *emission angular function* we have to integrate the two-dimensional emission function $I(\alpha,\omega)$ [for its definition, see text after Eq. (14)] over frequency, assuming SR intensity to be a frequency-independent value $I_{\mathrm{SR}}(\omega) = \mathrm{const}$ over the whole range of the nuclear resonance. The *emission angular function* is then given by the following integral:

$$I(x) = \int_{-\infty}^{+\infty} dv\, I\,(x,v)\,, \tag{15}$$

where in the intensity function the angular and frequency variables are replaced adequately: $x = \Delta\theta \propto \alpha$ and $v = \hbar\omega/(\Gamma_0/2)$. One should underline that the expression of Eq. (15) gives the emission angular dependence integrated over the whole resonance range. The emission angular functions for different magnitudes of the internal magnetic field are displayed in Fig. 5. The curve on the bottom panel of Fig. 5 having a symmetric shape represents the angular dependence of emission at room temperature. The center of angular range of pronounced emission is shifted with respect to the angle given by the original Bragg reflection law by 15.5 μrad. This shift is due to refraction of the incident beam at the entrance into the crystal. The width of the reflectivity curve is very small, 5 μrad.

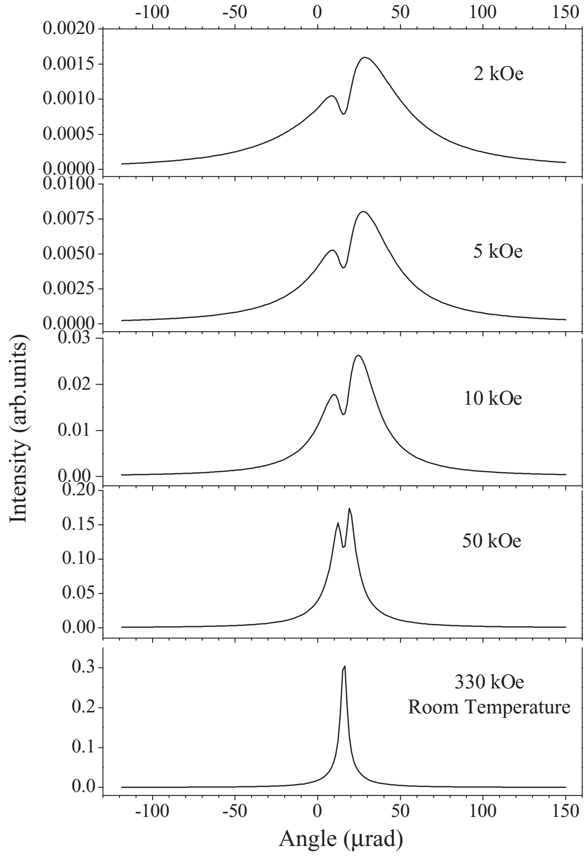

FIG. 5. The emission angular dependence of γ radiation from the IB crystal integrated over the whole resonance range. The angular setting of the IB crystal is changed in the vicinity of Bragg angle for pure nuclear reflection (333). The angular functions are displayed for different values of the internal magnetic field decreasing from the bottom to the top in approaching Néel temperature.

When heating the crystal toward Néel temperature the breadth and shape of the emission angular function is drastically changed. Three main features can be recognized [25]:

(a) significant decrease of the emitted intensity,

(b) strong broadening of the angular range of emission,

(c) creation of the double-hump structure of the angular curves with the dip exactly at the Bragg angle corrected for refraction.

At the lowest field (i.e., the highest temperature of the crystal) the emission intensity is only of the order of 10^{-2} of the intensity at room temperature. Such diminution of the coherent emission near Néel temperature was expected because of the destructive nature of interference at this temperature.

Along with the decrease of the coherent emission the angular range of emission is being significantly enlarged: from ~5 μrad at the field of 330 kOe (the bottom panel in Fig. 5) up to ~60 μrad at the field of 2 kOe (the upper panel in Fig. 5). This happens because the strong off-resonance wings of nuclear scattering (located mainly in the narrow angular interval around the exact Bragg position, i.e., around the peak of the rocking curve) [see Figs. 4(a) and 4(b)] become heavily suppressed by destructive interference when temperature approaches T_n [Fig. 4(c)]. In contrast, the wider angular distribution of the on-resonance scattering is less affected by destructive interference [Fig. 4(c)]. Thus, it provides the wider rocking curve around T_n. It is of interest to note that a further decrease of the field and of the related emission intensity is not accompanied any longer by a change of the shape and the width of the angular curve. A kind of saturation is reached in the breadth of the angular range of emission of γ rays over the entire resonance region near the Néel point.

Figure 4(c) shows that the outer wings of the landscape fall abruptly in the narrow angular interval near the Bragg angle. Computer analysis of the emission function shows that the wings are shifted out of the immediate Bragg range more and more as the collapse of the hyperfine structure occurs. They start therefore to give their contributions to the emitted radiation only when the angle of incidence is shifted from the central zone to the sides. This is the reason for the formation of the double-hump structure and the appearance of the dip in the emission angular function.

The angular distribution of the emitted γ radiation is determined both by the emission angular function and by the instrumental function (i.e., by the angular distribution of synchrotron radiation in the incident beam). When the angular divergence of the exciting radiation is large in comparison with the angular width of the range of emission, the emission occurs throughout the whole allowed range. If the SR intensity is a constant value in this range, the angular distributions of the emitted γ radiation just repeat those depicted in Fig. 5. In the opposite case of very small divergence of the exciting radiation in comparison with the angular width of emission, the angular distribution of γ radiation reproduces the instrumentation function form. To get the angular distribution of the emitted radiation in an intermediate case one must find the product of the emission angular function $I(x)$ and of the instrumental function at an arbitrary angle of incidence x_p of the exciting synchrotron radiation. An example of the angular distribution of the emitted radiation is shown in Fig. 6, assuming the instrumental function to be of Gaussian form $F(x,x_p) = \frac{1}{\sigma\sqrt{2\pi}}\exp\{-\frac{(x-x_p)^2}{2\sigma^2}\}$. The nuclei are excited by SR exactly at the dip of the emission angular function, $x_p = 15.5$ μrad and $2\sigma = 10$ μrad. The angular distribution of γ radiation emitted in the vicinity of Néel temperature for the internal magnetic field of 2 kOe is compared with the instrumental angular function. As seen in the figure, under the considered real conditions, the angular breadth of the emitted radiation exceeds slightly the angular width of the instrumental function. The top of the distribution is slightly modulated by the emission angular function.

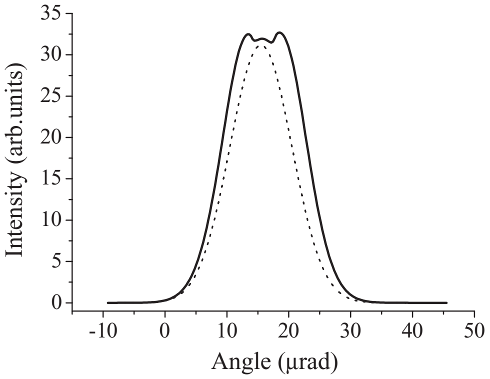

FIG. 6. Angular distribution of the emitted γ radiation (solid line); angular distribution of the exciting synchrotron radiation (dots) (see text). The first distribution is scaled in intensity for comparison with the second one. The crystal is set at the position of angular dip (top panel in Fig. 5).

We turn now to the energy distribution of the emitted γ radiation for a fixed angle of incidence of the exciting SR beam. At the beginning we consider a simple model of the destructive inter-resonance interference. As shown in Ref. [13], due to the combined multispace interference only two resonance lines survive close to Néel temperature. They belong to the third and sixth resonances in the original hyperfine structure in the ^{57}FeBO$_3$. The energies of the relevant transitions nearly coincide and the strengths of the lines are almost equal. Thus the spectrum in our model can be presented by the sum of two Lorentzians, each renders a single line radiation emitted at a separate resonance transition,

$$L(v,v_1 - v_2) = \sum_{k=1,2}\left|A_k\frac{1}{(v-v_k)-i}\right|^2 \quad \text{with } A_1 = -A_2. \tag{16}$$

As $v_2 \to v_1$, which corresponds to a collapse of the hyperfine structure, the emission intensity [as the integrand in Eq. (15)] vanishes. Under these conditions the double-peak structure is being transformed into a pseudosingle line, whose shape is given approximately by the following expression:

$$L(v,\delta) = \frac{\delta^2}{[(v-v_1)^2+1]^2}, \tag{17}$$

where $\delta = v_1 - v_2$. Thus the energy distribution is presented in our model by a *Lorentzian-squared function*. The line width in this case is less than Γ_0, namely ~0.64Γ_0. One should note that the interference is constructive at the energies lying in between the resonance ones v_1 and v_2, while, in contrast, it is destructive on both left and right outer sides of resonance region [the amplitudes in Eq. (16) tend to cancel each other there]. Whence, γ-ray emission completely disappears when $\delta \to 0$ (above Néel temperature). However, in the real case the application of a small external magnetic field restores the antiferromagnet structure of the crystal and γ-ray coherent emission resumes [11]. Due to coherent effects the real width of the energy distribution Γ_{coh} can be larger than Γ_0.

To obtain the energy distribution of the emitted γ radiation at the angle of incidence of x_p one should calculate the

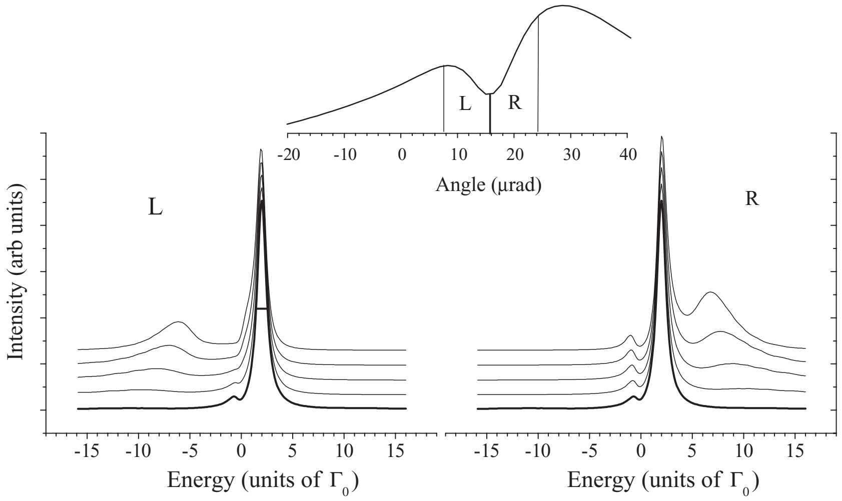

FIG. 7. Energy distributions of the emitted γ radiation at different angles of incidence of the exciting SR in the vicinity of the dip zone of the emission angular function for the (333) reflection and for the internal magnetic field of 2 kOe. The dip zone (taken from Fig. 5) is shown on the upper panel. The energy distributions on the lower panels refer to the left and the right sides of the dip zone, L and R respectively, as shown on the upper panel. The energy distribution at the exact dip position is displayed on both L and R panels (bold line curves). Each next distribution corresponds to an angular shift of the crystal from the dip position by 5 μrad. For better visualization the energy spectra are equally spaced along the vertical axis.

following integral:

$$\tilde{I}_{x_p}(v) = \int_{-\infty}^{+\infty} dx\, F(x,x_p) \cdot I(x,v). \tag{18}$$

All the values entering into Eq. (18) are defined above. Several energy distributions of γ radiation emitted near Néel temperature at different angles of incidence of the SR are displayed in Fig. 7. The central part of the emission angular function around $x_p = 15.5$ μrad is shown on the upper panel in Fig. 7, where the considered angular interval is limited by the L and R bars. It is mostly the region in between the two humps of the angular curve. The divergence of the exciting SR beam is taken as 5 μrad.

The step in change of the angle of incidence is of the same value. The energy distributions of the emitted γ radiation are shown on the lower panels. The distributions corresponding to the shifts toward the lower hump of the emission angular function (to the left of the dip zone) are denoted by L and those toward the higher hump (to the right of the dip zone) are denoted by R. The energy distribution of the emitted γ rays in the case of excitation of the nuclear array at the exact dip position is represented by the bold line curve on both L and R graphs.

The nature of the double-hump structure in the emission angular function prompts the idea to select just the dip zone for obtaining a single-line SM radiation spectrum. Indeed, as seen from the figure, in this range it is predominantly a single line having a width close to Γ_0 (horizontal bar on the half-height). A strongly suppressed satellite is noticed on the left-hand side of the main peak. When moving off the center of the angular curve to its left hump a broader line is being formed in the range of the lower energies of the radiation spectrum. Its relative contribution is rising as the angular shift is increasing. When moving off the center of the angular curve toward its right hump the changes of the radiation spectrum are mostly the same but now a broader line appears at the right-hand side of the central maximum and the small satellite is not smoothing out as in the L distributions. Appearance of the side broad lines in both L and R spectra is due to excitation of the nuclear array at the angles of incidence at which the wings the emission landscape in Fig. 4(c) are already touched.

Finally we come to the angular resolved time distributions of the emitted γ radiation. They were calculated by performing the following integration

$$\tilde{I}_{x_p}(t) = \int_{-\infty}^{+\infty} dx\, F(x,x_p) \left| \int_{-\infty}^{+\infty} dv\, E(x,v) \exp\{ivt/2t_0\} \right|^2, \tag{19}$$

where t is real time and $t_0 = \hbar/\Gamma_0$ is the natural lifetime of the excited nuclear state. The inner integral represents the inverse Fourier transform of the energy distributions of the emitted radiation amplitudes. The obtained time distributions are displayed in Fig. 8. This figure is delineated in the same way as the former one. All time dependencies there correspond to the energy distributions shown in Fig. 7. The time dependence of the emitted γ radiation in the case of excitation of the nuclear array at the exact dip is marked by the bold lines on both L and R graphs. The nonexponential shape of this dependence reveals the true nature of a single-line spectrum obtained nearby the Néel point. In fact it is a pseudosingle line formed in the process of the combined interference of radiation paths in the geometric space, and in energy and spin domains. In particular, the γ-ray waves emitted by nuclei in the unit cell right upon excitation cancel each other, because these waves are of equal amplitudes and opposite in sign due to the phase shift between them of π at the zero time. The relative phase between the waves is changing due to a difference in their carrier frequencies with time toward their constructive interference, therefore a quantum beat pattern could be observed. However, at the same time the coherent decay of the excited state is proceeding, so that the quantum beat and decay processes are overlapped in time. In our model of interference of the two Lorentzian lines, see Eq. (16), using the inverse Fourier transform, we can obtain the following time dependence:

$$I(t) = 2\,[1 - \cos(\omega_1 - \omega_2)\,t]\exp(-t/t_0), \tag{20}$$

where quantum beating and decay are presented by the pre-exponential factor and the exponential one, respectively. Quantum beat period here is $T = 2\pi t_0/(\omega_1 - \omega_2)$. The resultant pattern depends strongly on the relation between the characteristic times of the two processes, the beat period T and

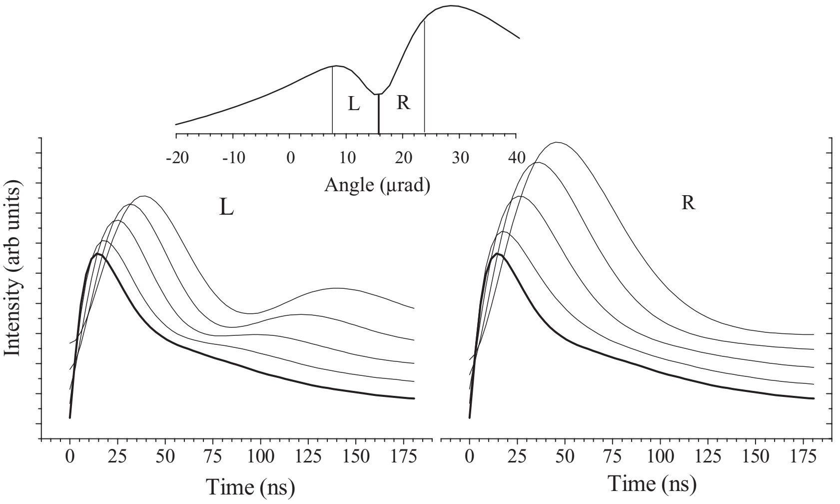

FIG. 8. Time distributions of the emitted γ radiation at different angles of incidence of the exciting SR in the vicinity of the dip zone of the emission angular function for the (333) reflection and for the internal magnetic field of 2 kOe. The dip zone (taken from Fig. 5) is shown on the upper panel. The time distributions on the lower panels refer to the left and the right sides of the dip zone, L and R respectively, as shown on the upper panel. The time distribution at the exact dip position is displayed on both L and R panels (bold line curves). Each next distribution corresponds to an angular shift of the crystal from the dip position by 5 μrad. For better visualization the time distributions are equally spaced along the vertical axis.

the natural decay time t_0. In the case where the beat period and decay time are of the same order the two processes compete.

In the real case one should consider the relation between the beat period and the characteristic time of the coherent emission t_{coh}. In the vicinity of Néel temperature the beat period T can be several times larger than t_{coh}, since in this temperature range the hyperfine splitting is already a fraction of the breadth of the coherent resonance line. The transition from destructive to constructive interference proceeds here slower than the decay. In this approximation the following time dependence is valid: $I(t) \approx t^2\exp(t/t_{\mathrm{coh}})$. The form of the time dependencies in Fig. 8 is still determined by the competing processes. Increase of the intensity due to positive-going inter-resonance interference is compensated by the speeded up coherent emission. This competition results in the formation of the emission maximum in the time dependencies. When approaching the times of fully constructive interference most of the stored energy is released already through the incoherent channels [12].

When moving from the central angular zone toward the humps the time distributions are determined in addition to the discussed reasons by the interference of the narrow central component with the broader lines at the sides in L and R graphs of Fig. 7.

V. SUMMARY

Electronically forbidden but nuclear-allowed Bragg reflections can be employed to generate the recoilless γ radiation by exciting a nuclear array to its isomer level with the help of the synchrotron radiation. Pure nuclear reflections exist owing to a strong spin dependence of nuclear scattering in the presence of hyperfine fields in crystals. This way a source of Mössbauer radiation alternative to the radioisotope sources can be realized. The coherent excitation of the nuclear array leads to the creation of nuclear exciton polariton states, which generate at the exit of the crystal the coherent γ radiation free of a nonresonant contribution.

A particular case of pure nuclear reflection is considered where a single line ^{57}Fe Mössbauer radiation is generated. It is accomplished in an antiferromagnet ^{57}FeBO$_3$ crystal [iron borate (IB) crystal] heated up to the vicinity of its Néel temperature.

When considering the interference of radiation while nuclei in the unit cell of the IB crystal de-excite one can find 48 contributions into the interference amplitude. Two contributions come from the de-excitation of the two nuclei present in the unit cell. Each of them contains six contributions in the energy domain where nuclear levels are split due to combined magnetic and electric hyperfine interaction in the IB crystal. Finally near Néel point where the magnetic dipole and electric quadrupole interactions in the IB crystal are of comparable strength the nuclear sublevels in the excited state become strongly mixed in spin projections. The two projections of nuclear spin are allowed at each sublevel. Therefore each of the six contributions in the energy domain involves in addition the four contributions in the spin domain. Thus the combined multipath interference in geometric space, in energy, and spin domains results in the formation of a pseudosingle-line resonance structure which provides a basis for performing a single-line synchrotron Mössbauer (SM) source.

Mutual interference of the propagating and Bragg reflected waves inside the crystal produce a resultant wave field (WF) with standing-wave-type structure. In this way the standing-wave mode of the nuclear exciton polariton is realized under conditions of Bragg diffraction. One obtains two solutions for the WF amplitudes. Both are modulated in the direction perpendicular to the reflecting planes in such a way that the WF1 experiences an anomalously weak nuclear absorption, while the WF2, on the contrary, experiences an anomalously strong absorption. In the limit of a semi-infinite crystal only the WF1 survives. A strong suppression of inelastic scattering channels for this wave field is favoring an enhanced γ-ray emission nearly without internal conversion. At the exit of the crystal a coherent beam of resonant γ radiation is formed.

For nuclear resonant Bragg reflections the emission from a crystal containing a nuclear array exhibits a combined angular and energy dependence. In the case of the IB crystal the dependence undergoes a dramatic change in heating the crystal from room to Néel temperature. Near Néel point its shape is transformed significantly both in energy and in angular dimensions. The multiline spectrum of the emitted radiation collapses while the angular range of emission extends. In the vicinity of Bragg angle a pseudosingle-line resonance structure is formed, which is created by the internuclear interference (in geometrical space) as well as by a strong inter-resonance (in energy domain) and intraresonance (in spin domain) interference of radiation components.

The emission angular function, which represents the emission intensity for different angular settings of the crystal near Bragg angle in the approximation of a plane incident wave, strongly broadens and transforms to a double-hump structure with a central dip in between of the peaks. The breadth of the angular distribution increases by more than one order of magnitude in heating the crystal from room to Néel temperature. However, in the very vicinity of Néel temperature the saturation in angular breadth sets in. Most interesting is the double-hump shape of the angular distribution in this range. The two emission branches originate due to the Lorentzian form of the scattering amplitude. Off resonance, the nuclear scattering amplitude is approximately real. The latter, being an uneven function of energy deviation off resonance, is responsible for the existence of the two wings for the emission function on the angular-energy plane in Fig. 4 (see also Ref. [23]). There is a gap in the vicinity of the Bragg angle where the wings are negligibly weak. Just in this angular range the spectrum of the emitted radiation consists predominantly of a single line having a width of about the natural resonance line width Γ_0.

The time distribution reveals the true structure of the single-line spectrum of the emitted radiation. In fact the single line consists of two unresolved lines of the hyperfine structure in the vicinity of Néel temperature. Due to the transition from the destructive mode of interference between the hyperfine components to the constructive one an initial rise of intensity is observed. However, competing process of nuclear de-excitation prevents reaching the conditions of the entirely constructive interference. Finally, when the times of the constructive interference come, most of the energy stored by nuclei turn out to be released already through the incoherent channels [12]. For this reason the time distributions exhibit a broad maximum of low intensity.

The analysis of the coherent emission of γ rays from a crystal of iron borate, and namely, of the emission angular function, the energy and time distributions of the emitted radiation, is necessary for further elaboration of the ^{57}Fe Synchrotron Mössbauer Source—the device which provides a collimated beam of intense and polarized γ radiation in an energy bandwidth of nano-electronvolts, the nuclear resonance natural level width.

[1] G. V. Smirnov, U. van Bürck, W. Potzel, P. Schindelmann, S. L. Popov, E. Gerdau, Y. V. Shvydko, H. D. Rüter, and O. Leupold, Phys. Rev. A **71**, 023804 (2005).

[2] G. V. Smirnov, U. van Bürck, J. Arthur, G. S. Brown, A. I. Chumakov, A. Q. R. Baron, W. Petry, and S. L. Ruby, Phys. Rev. A **76**, 043811 (2007).

[3] M. Haas, Phys. Lett. A **361**, 391 (2007).

[4] Y. Kagan, A. M. Afanas'ev, and V. G. Kohn, J. Phys. C **12**, 615 (1979).

[5] G. T. Trammell, Proc. Intern. Atomic Energy Agency Symp. on Chemical Effects of Nuclear Transformations **1**, 75 (1961).

[6] V. A. Belyakov and Y. M. Ayvazian, JETP Lett. **7**, 368 (1968).

[7] V. A. Belyakov and Y. M. Ayvazian, JETP Lett. **9**, 393 (1969).

[8] G. V. Smirnov, V. V. Sklyarevskii, R. A. Voscanian, and A. N. Artem'ev, JETP Lett. **9**, 70 (1969).

[9] R. M. Mirzababaev, G. V. Smirnov, V. V. Sklyarevskii, A. N. Artem'ev, A. N. Izrailenko, and A. V. Babkov, Phys. Lett. A **37**, 441 (1971).

[10] E. Gerdau, R. Rüffer, H. Winkler, W. Tolksdorf, C. P. Klages, and J. P. Hannon, Phys. Rev. Lett. **54**, 835 (1985).

[11] G. V. Smirnov, M. V. Zelepukhin, and U. van Bürck, JETP Lett. **43**, 352 (1986).

[12] A. I. Chumakov, M. V. Zelepukhin, G. V. Smirnov, U. van Bürck, R. Rüffer, R. Hollatz, H. D. Rüter, and E. Gerdau, Phys. Rev. B **41**, 9545 (1990).

[13] G. V. Smirnov, Hyperfine Interact. **125**, 91 (2000).

[14] G. V. Smirnov, U. van Bürck, A. I. Chumakov, A. Q. R. Baron, and R. Rüffer, Phys. Rev. B **55**, 5811 (1997).

[15] Q. A. Pankhurst, N. S. Cohen, L. F. Barquin, M. R. Gibbs, and G. V. Smirnov, J. Non-Cryst. Solids **287**, 81 (2001).

[16] T. Mitsui, N. Hirao, Y. Ohishi, R. Masuda, Y. Nakamura, H. Enoki, K. Sakaki, and M. Seto, J. Synchrotron Radiat. **16**, 723 (2009).

[17] C. G. Shull, W. A. Strauser, and E. O. Wollan, Phys. Rev. **83**, 333 (1951).

[18] A. S. Borovik-Romanov and V. I. Ozhogin, Sov. Phys. JETP **12**, 18 (1961).

[19] Y. Kagan, Hyperfine Interact. **123/124**, 83 (1999).

[20] J. P. Hannon and G. T. Trammell, Hyperfine Interact. **123/124**, 127 (1999).

[21] A. M. Afanas'ev and Y. Kagan, Sov. Phys. JETP **21**, 215 (1965).

[22] G. V. Smirnov, Hyperfine Interact. **27**, 203 (1986).

[23] U. van Bürck, G. V. Smirnov, R. L. Mössbauer, H. J. Maurus, and N. A. Semioschkina, J. Phys. C **13**, 4511 (1980).

[24] Y. V. Schvyd'ko and G. V. Smirnov, J. Phys. Condens. Matter **1**, 10563 (1989).

[25] G. V. Smirnov, Preprint IAE-6614/9 (2009).